Health Monitoring of Tree Trunks Using Ground Penetrating Radar

Iraklis Giannakis, Fabio Tosti, *Senior Member, IEEE*, Livia Lantini, and Amir M. Alani

***Abstract*— Ground penetrating radar (GPR) is traditionally applied to smooth surfaces in which the assumption of half-space is an adequate approximation that does not deviate much from reality. Nonetheless, using GPR for internal structure characterization of tree trunks requires measurements on an irregularly shaped closed curve. A typical hyperbola fitting has no physical meaning in this new context since the reflection patterns are strongly associated with the shape of the tree trunk. Instead of a clinical hyperbola, the reflections give rise to complex-shaped patterns that are difficult to be analyzed even in the absence of clutter. In this paper, a novel processing scheme is described which can interpret complex reflection patterns assuming a circular target subject to any arbitrary shaped surface. The proposed methodology can be applied using commercial hand-held antennas in real time, avoiding computationally costly tomographic approaches that require the usage of custom-made bespoke antenna arrays. The validity of the current approach is illustrated both with numerical and real experiments.**

***Index Terms*— Ground penetrating radar (GPR), hyperbola fitting, tree, trunk.**

I. Introduction

MONITORING wood materials is of great importance with both industrial and environmental applications [1], [2]. Preserving cultural-heritage objects [1], evaluating the structural stability of wooden-based structures [1], and assessing the health conditions of living trees [3] are amongst the areas in which wood imaging has been successfully applied. A direct method for monitoring the internal structure of the wood is core drilling [4]. This is a time-consuming intrusive methodology that can potentially damage the tree. To that extent, nondestructive testing (NDT) has been suggested in an effort to provide a reliable and a non-intrusive scheme for estimating the internal structure of wood.

NDT utilizes the received information in an effort to indirectly map the physical properties of the tree trunk. Amongst the investigated properties are the water content, the dielectric properties, the elastic properties, and the density [1]. From the investigated properties, it is apparent that a wide range of NDT and geophysical methods need to be applied, from estimating the elasticity of the wood by mechanical means [5], minimum intrusive techniques such as drilling resistance [6] and electrical resistivity tomography (ERT) [7], [8] to ultrasound tomography [9], thermography [10]–[12] and more sophisticated techniques such as X-ray computed tomography (CT-scan) [13] and neutron imaging [14], [15]. These techniques differ with respect to accuracy, limitations, and practicality. For example, CT-scan can provide a very accurate and detailed image of the internal structure of the tree; nonetheless, when field measurements and fast results are required, CT-scan is neither attainable nor commercially appealing.

A particularly challenging application of wood monitoring is assessing the health condition of living trees [3]. Monitoring the living trees has some inherited constraints arising from the nature of the acquisition. Any methodology proposed to tackle this problem should have reasonable computational requirements in order to be applicable in large-scale projects such as forestry applications. In addition, detecting tree decays requires extensive field measurements in nontrivial environments. Therefore, any equipment necessary for the acquisitions should be portable and easily deployable to the site of interest. In that context, ground penetrating radar (GPR) has been suggested as a potential methodology to assess the health conditions of trees in a reliable and efficient manner [3], [16].

Due to the cylindrical shape of the trees, tomographic approaches are particularly appealing from a mathematical point of view. Microwave imaging of cylindrical bodies has been widely applied for biomedical applications [17] using inversion schemes primarily based on linear approximations [20], [21]. This framework has been extrapolated for assessing the internal structure of tree trunks with promising results [19]. In the same context, ray-based tomography using GPR has also been tested for detecting anomalies inside tree trunks [18]. To our knowledge, full-waveform inversion (FWI) applied on tree monitoring has not been reported in the literature. FWI is a powerful tool for interpreting GPR data [22]–[24]; nonetheless, its high computational requirements combined with the need for an accurate antenna model incorporated in the forward solver [25] make the implementation of FWI to GPR a laborious process with limited commercial applications.

Tomographic approaches, apart from being computationally demanding, they also require a full set of measurements with multiple transmitters and receivers often using custom-made bespoke systems [19]. This deviates from the norm since GPR surveys traditionally employ commercial antennas using the common-offset method of measurements [26]. In that context, in an effort to develop a commercially appealing methodology,

Manuscript received February 5, 2019; revised May 21, 2019; accepted May 26, 2019. Date of publication June 20, 2019; date of current version September 25, 2019. This work was supported by the Lord Faringdon Charitable Trust under Grant 1084690. *(Corresponding author: Iraklis Giannakis.)*

The authors are with the School of Computing and Engineering, University of West London, London W5 5RF, U.K. (e-mail: iraklis.giannakis@uwl.ac.uk; fabio.tosti@uwl.ac.uk; livia.lantini@uwl.ac.uk; amir.alani@uwl.ac.uk).

Color versions of one or more of the figures in this article are available online at http://ieeexplore.ieee.org.

Digital Object Identifier 10.1109/TGRS.2019.2920224

a signal processing approach is presented in the current paper that estimates the size and the coordinates of tree decays using common-offset commercial systems.

Circular targets subject to a homogeneous half-space give rise to hyperbolic features in the measured B-Scans. Hyperbola fitting is a mainstream processing approach in the GPR community [26] due to its simplicity and effectiveness when the assumptions are met. Hyperbola fitting can be interpreted as a typical minimization of the distance between given points and a hyperbola [27]. Nonetheless, due to the noise and the clutter inherently present in B-Scans, an automatic hyperbola fitting is a challenging task that often requires preprocessing prior to any fitting scheme [28], [29]. In addition, similar hyperbolic patterns can emerge for different sets of target's radii and permittivity values, introducing nonuniqueness to the problem [28]. Knowing the velocity of the medium, or assuming a point-target, Hough transform for hyperbolas can be utilized in an effort to map the distribution of the hyperbolas on a given B-Scan [26], [30], [31]. Hough transform can be seen as a brute force optimization that maps the given feature space and subsequently detects local minima that are identified as hyperbolas. The brute-force nature of the Hough transform makes this approach computationally demanding with a computational burden that expands geometrically when the resolution of the feature space is increased [29]. One of the most effective methods to reduce the feature space is to apply machine learning prior to Hough transform in order to detect sub-spaces that contain hyperbolas [32]. In [33], a Viola-Jones [34] detection scheme is applied in order to automatically detect areas in which hyperbolas are present. As it is stated in [29], the training process requires an extensive library of both positive and negative B-Scans in order for the classifier to be sufficiently trained.

All the methods mentioned above focus on circular targets buried in a homogeneous half-space. Evaluating the internal structure of cylindrical targets—like tree trunks—requires a more generic approach, since the assumption of half-space is no longer valid. Tree trunks are complicated structures and their shape differs based on age, species and environmental conditions [35]. The proposed scheme expands the traditional hyperbola fitting method [28], [29] from half-spaces to arbitrary complex shapes. Prior to that, a practical positioning approach should be established. Commercial GPR systems use a wheel-based system in order to associate each A-Scan with a specific distance from a given reference point. A wheel-based system of positioning is very practical when applied to line measurements. Nonetheless, plane measurements on irregular surfaces require a transformation of distance to 2-D coordinates. To that extent, an arc length approach is presented which can be applied in any plane measurements using a wheel-based positioning system.

Subsequently, image processing is applied in an effort to remove the ringing noise present in the B-Scans due to the layers of the tree. In this paper, two approaches have been chosen based on their performance and computational simplicity. The first one is the singular value decomposition (SVD) filter [36], [37] and the second one is the linear combination filter [38]. The image is then manually thresholded [29], [45] and a particle-swarm optimization (PSO) is used to fit the resulting anomaly, which can no longer be approximated with a hyperbola. Global optimizers such as PSO [39] overcome local minimal and make any initialization scheme unnecessary. Global optimizers can be seen as an intermediate step between convex nonlinear least squares fitting [27] and brute force approaches like Hough transform [30], [31]. Hence, PSO balances between efficiency and accuracy.

The suggested scheme has been successfully tested using commercial antennas in both synthetic and real data. This supports the premise that the proposed methodology is a reliable approach with minimum computational and operational requirements that can be applied in a straightforward manner to large scale forestry applications.

II. Reflection Patterns Using Common Offset Configuration

Typical GPR surveys take place in flat surfaces along a straight line. Each A-Scan is associated with a given position on that line based on the distance measured from a reference point. This distance is measured using a wheel-measuring device that is often incorporated in commercial GPR transducers. It is apparent that when the survey takes place in a straight line, distance can be trivially associated with a unique ordinate. This is not the case when the measurements are taken on irregular surfaces such as tree trunks. This problem is known as arc length parametrization and has a wide range of applications to computer graphics [40], [41].

A. Transforming Distance to Coordinates

In this section, an inclusive scheme based on [41] is described that can be applied in any arbitrary shaped host medium. Initially, the shape of interest is defined in x, y coordinates $\{x, y \in \mathbb{R} \mid x, y > 0\}$ discretized with an arbitrary nonuniform discretization step. The coordinates x, y are stored into the vectors $\mathbf{x} \in \mathbb{R}^n$ and $\mathbf{y} \in \mathbb{R}^n$, respectively, where n is the number of points used to discretise the shape of the host medium. The vector $\mathbf{t} = \langle t_1, t_2 \ldots, t_n \rangle$ $\{\mathbf{t} \in \mathbb{R}^n \mid 0 \leq t_i \leq 1\}$ is then defined which is going to be used as the arbitrary variable for the parametric representation of the shape of the host medium. The components of $\mathbf{t}$ increase linearly from zero to one with a constant step $(1/n)$, i.e., $\mathbf{t} = \langle 0, 1/n, 2/n \ldots .1 \rangle$. Using spline interpolation for the vectors $(\mathbf{y}, \mathbf{t})$, a set of polynomial functions are obtained. The latter maps y to t in a continuous manner

$$P_i : [t_i, t_{i+1}] \rightarrow \mathbb{R}. \tag{1}$$

Similarly, spline interpolation is used to map x with respect to t

$$Q_i : [t_i, t_{i+1}] \rightarrow \mathbb{R}. \tag{2}$$

Each of the functions P_i, Q_i are polynomials of the third order

$$P_i(t) = A_{p,i}t^3 + B_{p,i}t^2 + C_{p,i}t + D_{p,i} \quad \forall t \in [t_i, t_{i+1}] \tag{3}$$

$$Q_i(t) = A_{q,i}t^3 + B_{q,i}t^2 + C_{q,i}t + D_{q,i} \quad \forall t \in [t_i, t_{i+1}]. \tag{4}$$

Therefore, an arbitrary complex shape defined through discretized measurements can now be expressed in a vector form

as $\mathbf{F} = \langle P(t), Q(t)\rangle$. The shape can now be mapped with an arbitrary step since both x and y are expressed in a continuous manner.

The arc length of a planar curve in $\mathbb{R}^2$ written in a vector form $\mathbf{F}$ $\{\mathbf{F} \in \mathbb{R}^2\}$ is evaluated by [42]

$$s(\tau) = \int_0^\tau \left\| \frac{d\mathbf{F}}{dt} \right\| dt = \int_0^\tau \sqrt{\left(\frac{dP(t)}{dt}\right)^2 + \left(\frac{dQ(t)}{dt}\right)^2}\, dt \tag{5}$$

where

$$\frac{dP_i(t)}{dt} = 3A_{p,i}t^2 + 2B_{p,i}t + C_{p,i} \quad \forall t \in [t_i, t_{i+1}] \tag{6}$$

$$\frac{dQ_i(t)}{dt} = 3A_{q,i}t^2 + 2B_{q,i}t + C_{q,i} \quad \forall t \in [t_i, t_{i+1}]. \tag{7}$$

Arc length (5) has analytical solutions for limited number of curves (circle, catenary function, etc.). For complicated shapes such as tree trunks, the integral in (5) can be approximated numerically by

$$s(N\Delta t) \approx \sum_{k=0}^{N} \left\| \frac{d\langle P(k\Delta t), Q(k\Delta t)\rangle}{dt} \right\| \Delta t \tag{8}$$

where $\Delta t = (\tau/N)$. From (8), it is evident that

$$s(N\Delta t) \approx s((N-1)\Delta t) + \left\| \frac{d\langle P(N\Delta t), Q(N\Delta t)\rangle}{dt} \right\| \Delta t. \tag{9}$$

Equation (9) is an efficient way to compute $s(\tau)$ from its previous values without having to evaluate the summation in (8) for every time step. Using a spline interpolation, the values of τ can be mapped with respect to s in a continuous manner

$$T_i : [s_i, s_{i+1}] \to \mathbb{R}. \tag{10}$$

The function $T(s)$ approximates the value of the parameter τ with respect to the length s. Thus, for a given distance s the parametric variable τ associated with this distance can be estimated. Consequently, the positional vector $\mathbf{F} = \langle P(T(s)), Q(T(s))\rangle$ can now be connected to a given distance s. In that way, the distance measured by the wheel-measuring devices in commercial GPR antennas can be transformed to x, y coordinates using a limited amount of points to discretize the curve of interest.

B. Reflection-Arrival Travel-Time

The reflection-arrival travel-time is related to the distance—relative to a reference point—of each measurement via a hyperbolic equation [28]. The interpretation of the resulting hyperbola gives us an insight on the burial depth of the target, the velocity of the host medium and the size of the target [28]. The above holds true when the assumptions are met, i.e., when the host medium has a flat surface, when the target is circular and when the host medium is homogeneous. When the investigated surface is not flat, the resulting reflection patterns can no longer be approximated with a hyperbola [43], [44]. In [43] and [44], the reflection patterns that occur when the host medium is a cylinder are investigated and analyzed in detail. The scheme presented in [43] and [44] can be expanded to any arbitrary shape via

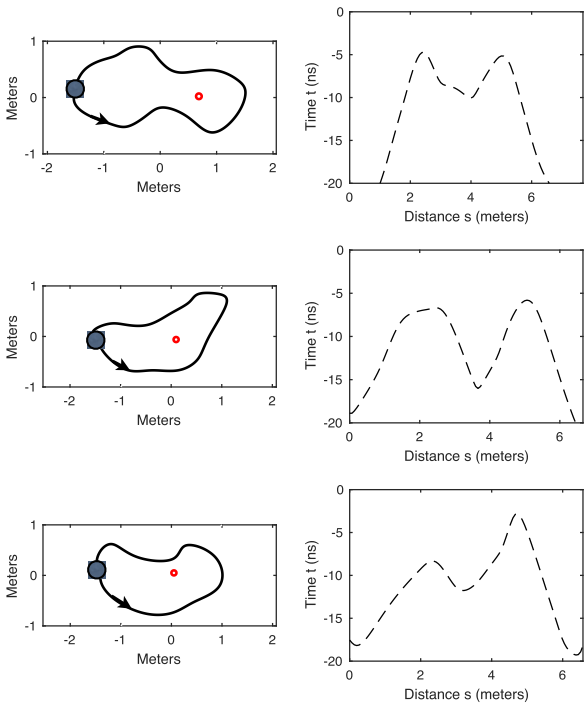

Fig. 1. (Left) With black line is the shape of the host medium. Gray circles: starting points of the measurements. The direction of the measurements is counterclockwise. Red circles: targets of interest. (Right) Arrival travel-time from the target is plotted with respect to the distance relative to the starting point (11).

$$t(s) = (\|\mathbf{F}(s) - \langle x_g, y_g\rangle\| - R)\frac{\sqrt{\epsilon}}{c_0} \tag{11}$$

where t is the time (in seconds), $\mathbf{F}(s) = \langle x_s, y_s\rangle$ is the positional vector (in meters) along the surface of the tree with respect to the distance from a reference point (see Section II-A), R is the radius of the cylindrical target (in meters), ϵ is the relative permittivity of the host medium, c_0 is the speed of light ($c_0 \approx 3 \cdot 10^8$, m/s), and $\langle x_g, y_g\rangle$ are the coordinates of the center of the target (in meters). As shown in Fig. 1, the relationship between s and t (11) for realistic tree trunks is complicated and highly related to the shape of the tree.

III. Processing Framework

The processing framework proposed in this paper consists of two parts. Initially, an SVD [36] and a linear filter [38] are used in order to reduce the ringing noise that is present to the measured B-Scans due to the layered nature of the tree trunk [35]. The postprocessed data are then manually thresholded and a PSO is used in order to estimate the origins and the size of the targets based on their reflection patterns.

A. Ringing Noise Removal

A generic tree trunk consists of five distinct layers, namely, bark, phloem, cambium, heartwood, and sapwood [35]. The aforementioned layers differ with respect to water content as

well as chemical composition and texture [35]. This results in dielectric contrasts that give rise to repetitive reflections contributing to the overall ringing noise. Due to that, two different methodologies are employed in an effort to reduce ringing noise and increase the overall signal to clutter ratio.

The data are collected along a given curve and each A-Scan $\mathbf{A}_s \in \mathbb{R}^w$ is a vector with size w which is measured at distance s from the starting point. The B-Scan $\mathbf{B} \in \mathbb{R}^{w\times S}$ is a 2-D matrix with $w \times S$ dimensions, where S is the number of measurements and $\mathbf{B} = \langle \mathbf{A}_{s_1}^T, \mathbf{A}_{s_2}^T \dots \mathbf{A}_{s_w}^T \rangle$ (T denotes the transpose sign). Ringing noise shows a similar behavior between A-Scans [45], [46]. This is the reason why a simple average removal [26] can often efficiently decrease ringing noise. Nonetheless, as it is stated in [36], other approaches such as SVD provide a more accurate and systematic way to reduce ringing noise in challenging scenarios with low signal-to-clutter ratio.

In SVD, the matrix $\mathbf{B}$ is decomposed into three matrices [36]

$$\mathbf{B} = \mathbf{U}\mathbf{M}\mathbf{V}^T \tag{12}$$

where $\mathbf{U} \in \mathbb{R}^{w\times w}$ and $\mathbf{V} \in \mathbb{R}^{S\times S}$ are orthogonal matrices and $\mathbf{M} \in \mathbb{R}^{w\times S}$ is a diagonal matrix that contains the eigenvalues of $\mathbf{B}$ arranged in a decreasing order. The large eigenvalues are associated with dominant repetitive features most often associated with ringing noise while small eigenvalues represent uncorrelated features such clutter and noise [47]. A typical SVD filter keeps the intermediate eigenvalues while setting the rest to zero

$$\overline{\mathbf{B}} = \mathbf{U}\overline{\mathbf{M}}\mathbf{V}^T \tag{13}$$

where $\overline{\mathbf{M}} \in \mathbb{R}^{w\times S}$, $\{\overline{\mathbf{M}}_{i,i} = 0 |\ \forall i\ [m_1, m_2]\}$ and m_1 and m_2 are the lower and upper eigenvalue-boundaries for the SVD filter.

SVD is a powerful tool for removing ringing noise, nonetheless as it is stated in [37], the performance of processing frameworks are case-dependent, and there is no conclusive approach that overperforms the rest. To that extent, a linear approximation of the signal is also considered as an alternative to SVD [38], [47]. The linear approximation uses a matrix $\mathbf{J} \in \mathbb{R}^{w\times q}$ that contains q number of randomly selected traces without the presence of any target. Subsequently, it is assumed that any A-Scan consists of the target's response ($\mathbf{E}_s$) plus clutter ($\mathbf{E}_c$)

$$\mathbf{A}_i = \mathbf{E}_{i,c} + \mathbf{E}_{i,s}. \tag{14}$$

The term clutter, here, is used to describe ringing noise, noise, and the cross-coupling between the transmitter and the receiver. Approximating $\mathbf{A}_i$ as a linear combination of the traces in $\mathbf{J}$ will result to a sufficient approximation of $\mathbf{E}_c$ and a poor approximation of $\mathbf{E}_s$. This is due to the fact that the clutter is correlated between the traces and it is easier to be modeled based on previous A-Scans. Using least squares, the linear coefficients of the matrix $\mathbf{J}$ are evaluated, and subsequently, the predicted clutter is subtracted from each A-Scan

$$\overline{\mathbf{A}}_i^T = \mathbf{A}_i^T - \mathbf{J}(\mathbf{J}^T\mathbf{J})^{-1}\mathbf{J}^T\mathbf{A}_s^T. \tag{15}$$

B. Model Fitting

This section presents the equivalent of "hyperbola fitting" to the more inclusive and generic reflection patterns that are expected in tree trunks.

Through a manual threshold, the anomaly of interest can be gathered in a set of points $M = \{(s_i, t_i) \in \mathbb{R}, |i = 1, 2 \dots z\}$, where z is the number of observations. Based on M and (11), the center $\langle x_g, y_g \rangle$ of the target, its radius R and the relative permittivity of the host medium ϵ are fine-tuned in order to minimize

$$\underset{x_g, y_g, \epsilon, R}{\operatorname{argmin}} \sum_{i=1}^{z} \left(t_i - \left(\|\mathbf{F}(s_i) - \langle x_g, y_g \rangle\| - R \right) \frac{\sqrt{\epsilon}}{c_0} \right)^2. \tag{16}$$

It is easy to show that (16) can be rewritten as

$$\underset{x_g, y_g, \epsilon, R}{\operatorname{argmin}} \sum_{i=1}^{z} \left(t_i - \|\mathbf{F}(s_i) - \langle x_g, y_g \rangle\| \frac{\sqrt{\epsilon}}{c_0} + R\frac{\sqrt{\epsilon}}{c_0} \right)^2. \tag{17}$$

From (17), it is apparent that the radius R and the relative permittivity ϵ form a nonunique product, which means that different sets of (R, ϵ) might result in similar outputs. Thus, in the presence of noise, the minimization in (17) is sensitive due to nonuniqueness. This phenomenon was derived experimentally in [28] for flat surface surveys.

To overcome this, the bulk relative permittivity of the tree trunk can be approximated using the two-way travel time from the reflection of the opposite side of the tree. Knowing the time required for the electromagnetic wave to travel a known distance, the mean relative permittivity can be evaluated in a straightforward manner. If the relative permittivity is not readily available, then the minimization in (17) can be executed subject to an idealized point target, i.e., for $R = 0$.

The function to be minimized in (17) is subject to multiple local miminal due to the nature of the problem as well as the inherited noise in the measured M. To avoid initialization and overcome local minimal, a global optimizer is used for executing (17). In this paper, PSO [39] is chosen due to its popularity in electromagnetics [48], [49] and geophysics [50]. Using a different global optimizer (i.e., genetic algorithms, ant colony optimization, etc.) will have minor differences on the overall performance and computational requirements of the detection scheme. PSO initially generates a number of particles u that are placed randomly in the optimization space. For the case that permittivity is known, each particle k is a vector $\mathbf{q}_k = \langle x_k, y_k, R_k \rangle \{\mathbf{q}_k \in \mathbb{R}^3\}$. The cost function is then evaluated for every particle and their positions are updated in an iterative manner

$$\begin{aligned} \mathbf{v}_k^\tau &= b_0\mathbf{v}_k^{\tau-1} + b_1V_1\left(\mathbf{q}_k^{\tau-1} - \mathbf{q}_{k,b}\right) + b_2V_2\left(\mathbf{q}_k^{\tau-1} - \mathbf{q}_g\right) \\ \mathbf{q}_k^\tau &= \mathbf{q}_k^{\tau-1} + \mathbf{v}_k^\tau \end{aligned} \tag{18}$$

where b_0, b_1, and b_2 are constants associated with the convergence rate and the ability of PSO to converge to global solutions. In general, large values of b_0 and small values of b_2 decrease the convergence rate and the probability of the algorithm to be trapped in local minimal. The parameters $V_1, V_2 \in [0, 1]$ are random numbers with a uniform distribution and $\tau \in \mathbb{Z}$ is the integer iteration number.

The vector $\mathbf{v}_k \in \mathbb{R}^3$ is the velocity in the three dimensions of $\mathbf{q}_k$. The vector $\mathbf{q}_{k,b}$ is the position $\langle x_k, y_k, R_k \rangle$ of the particle k in which the cost function got its minimum value until the iteration τ. Finally, the vector $\mathbf{q}_g$ is the position $\langle x, y, R \rangle$ in which the cost function from all the particles got its minimum value until the iteration τ. For this case—through trial and error—it is derived that $u = 50$ and $b_0 = b_1 = b_2 = 1$ balances between efficiency and accuracy.

IV. Numerical Experiments

In this section, the proposed methodology is tested on synthetic data. A second order in both space and time finite-differences time-domain (FDTD) [51] method is used in order to numerically evaluate Maxwell's equations for a given dielectric distribution. In an effort to accelerate the computations, gprMax [53], an open-source compute unified device architecture (CUDA)-based GPU engine [52] is employed. The spatial discretization step is assumed to be uniform throughout the grid and equal with $\Delta x = \Delta y = \Delta z = 0.001$ m. The time step Δt follows the Courant limit [51].

The dielectric properties of wood vary seasonally as well as with respect to the type of the tree [54]. In general, softwoods contain more water content compared to hardwoods. Consequently, the permittivity of softwoods is substantially higher than the one of hardwoods [54]. The permittivity is also related to the orientation of measurement, i.e., the tree trunk is an anisotropic material, with the lowest permittivity values observed perpendicular to the layering of the tree [54]. A typical tree trunk consists of five layers, namely, the bark, the phlem, the cambium cell layer, the outer, and inner sapwood and the heartwood [35]. In addition to these layers, thinner rings of dense material occur in a periodic manner and almost parallel to each other [35]. The water content of the aforementioned structures greatly varies between different types of trees. For example, hardwoods consist of a dry heartwood and saturated sapwood in contrast to softwoods for which both sapwood and hardwood are equally saturated [54]. Numerous attempts have been made to generate semiempirical models for the dielectric properties of trees similar to the semiempirical models that exist for soils [55]. Nonetheless, a conclusive formula is not yet to be derived due to the complexity of the tree structure and its multi-phase composition.

Experimental evidences support the premise that the permittivity of trees increases linearly with the increase of water content [56]. Electrolytes and cellulose seems to have a secondary effect [54]. Due to its water content and the bipolar nature of the latter, the relative permittivity of the tree trunk can be expressed as an extended Debye model [54], [57], [58]

$$\epsilon(\omega) = \epsilon_\infty + \frac{\Delta\epsilon}{1 + j\omega t_0} - \frac{\sigma}{j\omega\epsilon_0} \tag{19}$$

where $j = \sqrt{-1}$, ϵ is the relative permittivity of the material with respect to ω, ω is the angular frequency, ϵ_∞ is the relative permittiviy at infinity frequency, $\Delta\epsilon$ is the difference between the static relative permittivity and the relative permittivity at infinity frequency, t_0 is the relaxation time, and σ is the conductive term. In order to map the underlying relationship between the dielectric parameters in (19) and the water content of the trunk, the complex refractive index model (CRIM) [59] is used. The latter, assumes that the tree trunk is a two-phase material and its relative bulk permittivity equals with

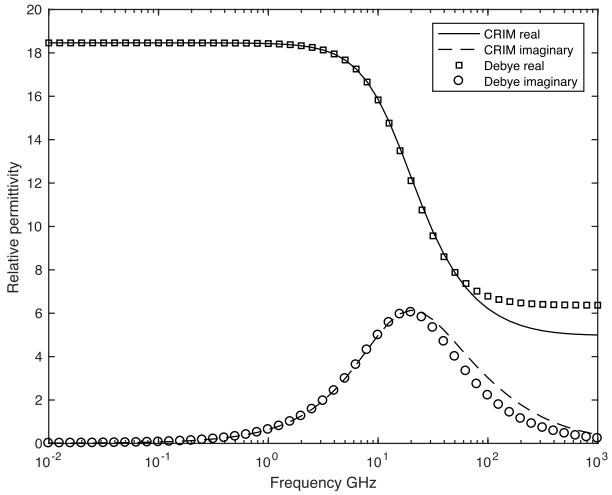

Fig. 2. Dielectric properties for the outer sapwood using CRIM model and its Debye equivalent. It is apparent that up to 10 GHz, one Debye pole is adequate for the approximation in (21).

$$\sqrt{\epsilon} = f_t\sqrt{\epsilon_t} + f_w\sqrt{\epsilon_w} \tag{20}$$

where ϵ is the relative bulk permittivity of the material, $\epsilon_t = 5$ is the relative permittivity of the solid phase of the tree, $\epsilon_w = 4.9 + 78/(1 + j\omega(9.23e - 12))$ is the dispersive relative permittivity of the water [55], and f_t and f_w are the volumetric fractions for the solid and the water phase, respectively ($f_t + f_w = 1$).

The CRIM model provides a simple and elegant way to express the bulk permittivity of a multi-phase medium with respect to its phases. Nonetheless, CRIM cannot be implemented directly to FDTD. To overcome this, (20) should be replaced with a function compatible with FDTD [60]. Given a specified volumetric water fraction, (20) can be approximated for a given frequency range $[\omega_l, \omega_u]$ by a multi-Debye pole

$$f_t\sqrt{\epsilon_t} + f_w\sqrt{\epsilon_w} \approx \epsilon_\infty + \sum_{h=1}^{H} \frac{\Delta\epsilon_h}{1 + j\omega t_{0,h}} \quad \forall\omega \in [\omega_l, \omega_u]. \tag{21}$$

The approximation above can be seen as a minimization problem

$$\underset{\Delta\epsilon_h, t_{0,h}, \epsilon_\infty}{\operatorname{argmin}} \sum_{i=l}^{u} \left(f_t\sqrt{\epsilon_t} + f_w\sqrt{\epsilon_w} - \epsilon_\infty - \sum_{h=1}^{H} \frac{\Delta\epsilon_h}{1 + j\omega_i t_{0,h}} \right)^2. \tag{22}$$

The minimization in (22) is executed using the hybrid scheme proposed in [49] for approximating Havriliak–Negami media with multi-Debye expansions. From Fig. 2, it is clear that one Debye pole ($H = 1$) is sufficient for approximating (21) for the frequency range of 0.01–10 GHz. In this numerical study, the water content of the tree layers is chosen such as to simulate saturated hardwoods like oaks or relatively dry softwoods like cedars. The Debye properties—derived

TABLE I
EXTENDED DEBYE PROPERTIES OF THE TREE LAYERS

Name	WC	ϵ_∞	$\Delta\epsilon$	σ $(\Omega^{-1}m^{-1})$	t_0 (sec)
Cabdium layer	40 %	6	18	1	9.23e-12
Outer Sapwood	30 %	6.1	12.36	0.033	9.23e-12
Inner Sapwood	25 %	5.9	9.66	0.02	9.23e-12
Rings	10 %	5.4	3.1	0.0083	9.23e-12
Heartwood	5 %	5.22	1.43	0.005	9.23e-12
Bark	0 %	5	0	0	9.23e-12

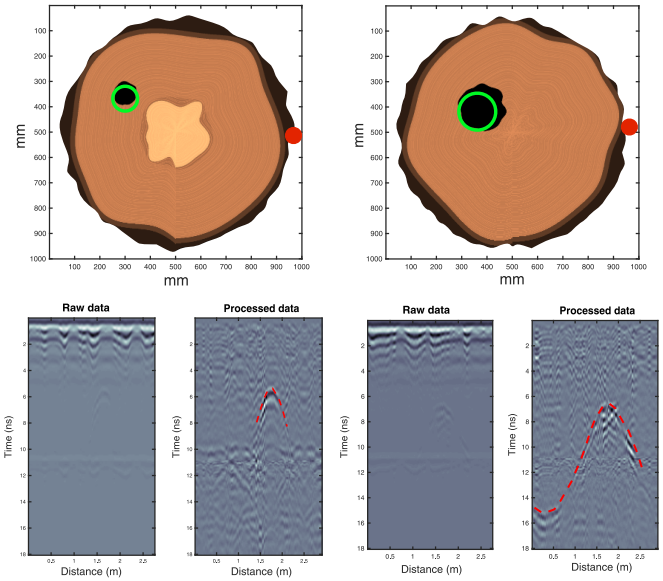

Fig. 3. (Left) One saturated hardwood and (Right) one semisaturated softwood are numerically simulated. Green lines: recovered tree decays using the suggested scheme. Red circles: starting point. The measurements are taken clockwise.

from (22)—of the tree layers used in this numerical study are shown in Table I. The conductivities are chosen based on typical values measured using ERT [61], [62].

A. Numerical Case Study

Hollow cavities throughout the tree trunk is a typical sign of tree decay and a robust indicator of the health status of the tree [63], [64]. Detecting cavities in a nondestructive manner is of high importance since extended cavities can compromise the stability and the structural integrity of the trunk leading to tree falls [63]. In this numerical study, the ability of the current scheme on detecting hollow cavities is investigated in two different numerical experiments.

The first case study is shown in Fig. 3. One saturated hardwood and one semisaturated softwood are investigated. For the saturated hardwood, the trunk consists of bark, cambium layer, outer sapwood, and heartwood. In the second case, the trunk consists of bark, cambium layer, and outer sapwood. For the excitation of the FDTD, a numerical equivalent of the commercial antenna GSSI 1.5 GHz is used [25], [65]. The excitation of the antenna is constrained to be parallel to one the Cartesian axes due to the arrangement of the fields in FDTD. Therefore, the models described in [25], [65] do not support tilted measurements. To overcome this, instead

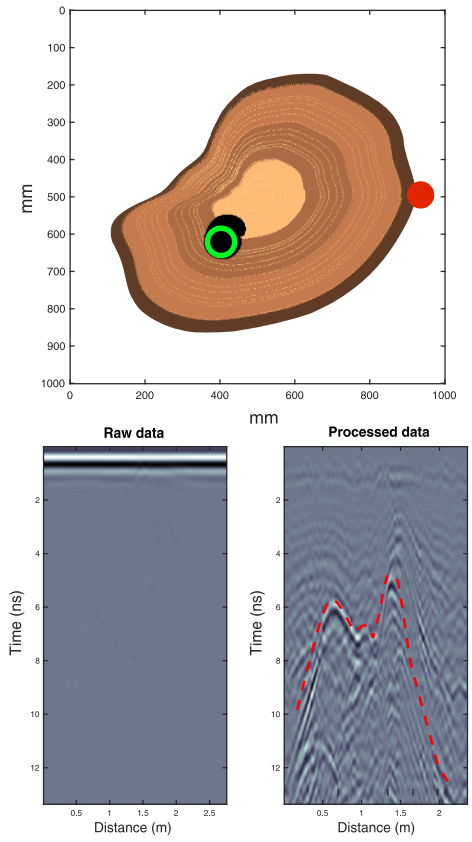

Fig. 4. Complex-shaped hardwood is numerically simulated. Green color: recovered position and radius of the tree decay. The starting measuring point is highlighted with red circle. The measurements are taken clockwise.

of rotating the antenna around the trunk, the trunk is rotated while the position of the antenna is fixed. The resulting B-Scan is processed using an SVD filter removing the six dominant eigenvalues. From Fig. 3, it is evident that the proposed scheme can accurately recover both the size as well as the location of the decay when the permittivity is known. For the current example, a mean relative permittivity $\epsilon = 18$ is assumed. If the permittivity is treated as an unknown in (17), the center of the target can be accurately estimated; nonetheless, its radius must be constrained to be zero in order to avoid nonuniqueness [28].

The second case study examines how the proposed scheme performs in complex-shaped tree trunks like the one shown in Fig. 4. A complex-shaped hardwood is examined with bark, cambium layer, outer sapwood, inner sapwood, and heartwood. Note that the complex shape of the trunk does not allow the tree to be rotated subject to a fixed antenna position. Due to that, the excitation source chosen for this case study is an ideal Hertzian dipole using a modulated Gaussian pulse with 1.5-GHz central frequency. Similar to the previous example, an SVD filter is applied to remove the ringing noise. The bulk relative permittivity is constrained to be equal to $\epsilon = 14$. The reflection patterns in the post-processed B-Scan are highly complicated and deviate from the typical hyperbolic features expected in GPR surveys. Patterns like these are difficult to be interpreted and can give the false impression of apparent layers or complex-shaped targets. The proposed methodology

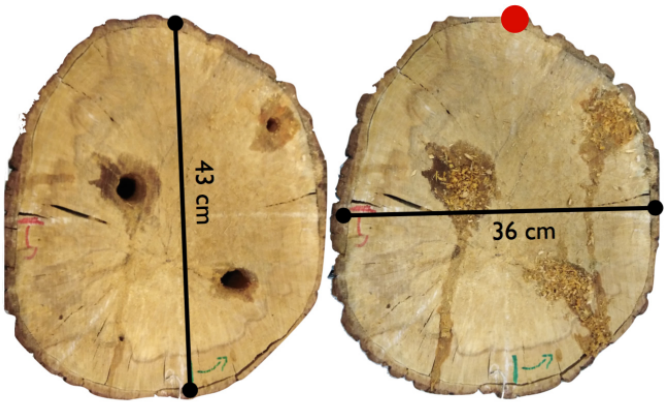

Fig. 5. (Left) Tree sample used in the current case study. (Right) Sawdust mixed with water used to fill the holes in order to simulate the liquid-filled chambers in the early stages of AOD. Red circle: starting point of the measurements. The measurements are taken counterclockwise.

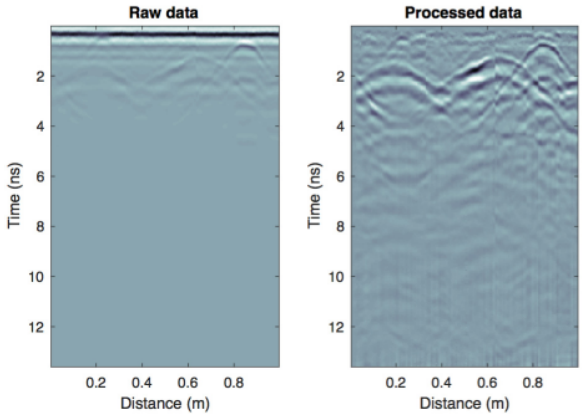

Fig. 6. (Left) Raw data collected using Aladdin with perpendicular polarization on the tree sample shown in Fig. 5. (Right) Postprocessed B-Scan.

manages to accurate recover both the position as well as the size of the decay by fitting the anomaly subject to the shape of the tree trunk.

V. Case Study

The suggested scheme is now applied to real data collected at the Faringdon Center at the University of West London. The investigated tree is the Quercus (oak), which is one of the most common tree species in Europe [66], [67]. Tree diseases are usually slow-progressing agents that gradually compromise the structure and the overall health of trees [68], [69]. Nonetheless, acute oak decline (AOD), a bacterial infection that affects oaks, leads to tree-mortality within few years [68], [69]. Incidents of AOD are increasing globally and AOD is now considered as a serious threat for the oak forests in Europe [68]–[70]. The early symptoms of AOD are small liquid-filled chambers within the tree trunk. The latter often reaches the outer bark, leading to a characteristic "bleeding" of the tree [68], [69].

In the current case study, the ability of the proposed scheme to detect AOD is tested under laboratory conditions. The host material is a dead oak with three drilled holes with different sizes. One hole with 2 cm radius and two holes with 4 cm radius. The gaps were subsequently filled with sawdust mixed with water in an effort to simulate the liquid-filled cavities that occur in AOD infected oaks (see Fig. 5). The antenna system used is the Aladdin hand-held dual-polarized antenna from IDS Georadar. Aladdin has been successfully applied in many high-frequency GPR applications [71], [72] and its size is suitable for measuring curved surfaces such as tree trunks. The measurements are taken counterclockwise every 1 cm using a measuring wheel. Using the approach described in Section II-A, the distance is transformed to coordinates. Zero-time removal, time-varying gain, and direct current (DC)-removal are initially applied to the raw data. Subsequently, an SVD and linear filter are used in an effort to reduce the ringing noise present in the B-Scan. In particular, two dominant eigenvalues are filtered out prior to linear filtering. The latter uses three randomly selected A-Scans to form the J matrix in (15).

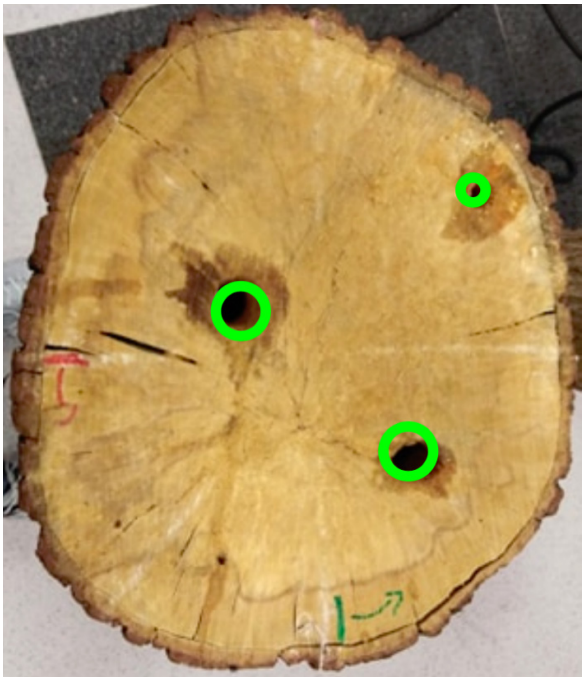

Fig. 7. Estimated coordinates and radii of the decays using the proposed detection scheme are illustrated with green circles. The holes in the tree were filled with saturated sawdust during the measurements (see Fig. 5). The holes are plotted empty in the current figure for comparison purposes.

Fig. 6 shows both the raw and the processed B-Scans using a perpendicular polarization. Three hyperbolic features are clearly visible from the postprocessed B-Scans. In order to estimate the position/size of the decay that best fits these features, the relative permittivity of the host material should be evaluated first. The bulk relative permittivity of the tree trunk was estimated $\epsilon \approx 3$ by measuring the two-way travel time from the opposite side of the trunk. A perfect conductor sheet was used in order to further enhance the reflection.

Fig. 7 shows the recovered coordinates and radii using the proposed fitting scheme. Three distinct and clearly visible patterns in the B-Scans were manually picked. Based on the shape of the tree and its mean relative permittivity, the minimization in (17) converged to three targets that best fit the data

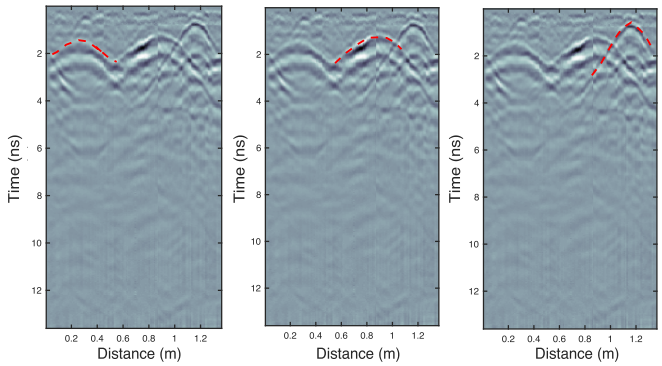

Fig. 8. Three different anomalies used to recover the coordinates and radii of the decays shown in Fig. 7.

(see Fig. 8). It is evident from Fig. 7 that using the suggested methodology, the positions as well as the radii of the decays can be successfully recovered in an efficient manner.

VI. Conclusion

A novel processing framework is described that can be applied to GPR surveys for assessing the internal structure of tree trunks. The proposed method can be coupled with commercial antennas with minimum computational and operational requirements. Numerical examples are provided to support the premise that tree decays can be successfully located using typical GPR surveys and thus avoiding tomographic approaches that require custom-made bespoke systems to be deployed on the site of interest. In addition, an experimental case study is presented in which the current scheme is successfully used to locate liquid-filled chambers associated with acute oat decline (AOD). The accuracy and the efficiency of the current methodology on detecting early signs of AOD make it commercially appealing for applications such as assessing the health status of trees on forestry applications.

Acknowledgment

The author would like to dedicate this paper to the memory of J. West, a friend, a colleague, a forester, a conservationist, and an environmentalist, who died following an accident in the woodland that he loved.

References

[1] P. Niemz and D. Mannes, "Non-destructive testing of wood and wood-based materials," *J. Cultural Heritage*, vol. 13, no. 3, pp. S26–S34, Sep. 2012.

[2] V. Bucur, *Nondestructive Characterization and Imaging of Wood*. Berlin, Germany: Springer, 2003.

[3] H. Lorenzo, V. Pérez-Gracia, A. Novo, and J. Armesto, "Forestry applications of ground-penetrating radar," *Forest Syst.*, vol. 19, no. 1, pp. 5–17, Apr. 2010.

[4] J. Ježová, L. Mertens, and S. Lambot, "Ground-penetrating radar for observing tree trunks and other cylindrical objects," *Construct. Building Mater.*, vol. 123, pp. 214–225, Oct. 2016.

[5] R. Pellerin and R. Ross, *Nondestructive Evaluation of Wood*. Madison, WI, USA: Forest Products Society, 2002.

[6] F. Rinn, F.-H. Schweingruber, and E. Schär, "RESISTOGRAPH and X-ray density charts of wood. Comparative evaluation of drill resistance profiles and X-ray density charts of different wood specie," *Holzforschung*, vol. 50, no. 4, pp. 303–311, Nov. 1996.

[7] L. R. Costello and S. L. Quarles, "Detection of wood decay in blue gum and elm: An evaluation of the Resistograph and the portable drill," *J. Arboriculture*, vol. 25, no. 6, pp. 311–318, Nov. 1999.

[8] S. A. A. Hagrey, "Electrical resistivity imaging of tree trunks," *Near Surf. Geophys.*, vol. 4, pp. 179–187, Jun. 2006.

[9] G. Deflorio, S. Fink, and F. W. M. R. Schwarze, "Detection of incipient decay in tree stems with sonic tomography after wounding and fungal inoculation," *Wood Sci. Technol.*, vol. 42, no. 2, pp. 117–132, Feb. 2008.

[10] A. Catena, "Thermography shows damaged tissue and cavities present in trees," in *Proc. 11th Int. Symp. Nondestruct. Characterization Mater.*, vol. 11, Jun. 2002, pp. 515–522.

[11] A. Catena, "Thermography reveals hidden tree decay," *Arboricultural J.*, vol. 27, pp. 27–42, May 2003.

[12] A. Catena and G. Catena, "Overview of thermal imaging for tree assessment," *Arboricultural J.*, vol. 30, pp. 259–270, Mar. 2008.

[13] Q. Wei, B. Leblon, and A. L. Rocque, "On the use of X-ray computed tomography for determining wood properties: A review," *Can. J. Forest Res.*, vol. 41, pp. 2120–2140, Oct. 2001.

[14] D. Mannes, P. Cherubini, E. Lehmann, and P. Niemz, "Neutron imaging versus standard X-ray densitometry as method to measure tree-ring wood density," *Trees*, vol. 21, pp. 605–612, Nov. 2007.

[15] D. C. Mannes, "Non-destructive testing of wood by means of neutron imaging in comparison with similar methods," Ph.D. dissertation, ETH Zürich, Switzerland, 2009.

[16] K. Takahashi and K. Aoike, "GPR measurements for diagnosing tree trunk," in *Proc. 17th Int. Conf. Ground Penetrating Radar (GPR)*, Switzerland, Jun. 2018, pp. 1–4.

[17] M. Pastorino, *Microwave Imaging*. Hoboken, NJ, USA: Wiley, 2010.

[18] L. Fu, S. Liu, and L. Liu, "Internal structure characterization of living tree trunk cross-section using GPR: Numerical examples and field data analysis," in *Proc. 15th Int. Conf. Ground Penetrating Radar*, Brussels, Belgium, Jun./Jul. 2014, pp. 155–160.

[19] F. Boero *et al.*, "Microwave tomography for the inspection of wood materials: Imaging system and experimental results," *IEEE Trans. Microw. Theory Techn.*, vol. 66, no. 7, pp. 3497–3510, Jul. 2018.

[20] Z. Miao and P. Kosmas, "Multiple-frequency DBIM-TwIST algorithm for microwave breast imaging," *IEEE Trans. Antennas Propag.*, vol. 65, no. 5, pp. 2507–2516, May 2017.

[21] C. Gilmore, A. Abubakar, W. Hu, T. M. Habashy, and P. M. van den Berg, "Microwave biomedical data inversion using the finite-difference contrast source inversion method," *IEEE Trans. Antennas Propag.*, vol. 57, no. 5, pp. 1528–1538, May 2009.

[22] A. Klotzsche, J. Van der Kruk, G. Meles, and H. Vereecken, "Crosshole GPR full-waveform inversion of waveguides acting as preferential flow paths within aquifer systems," *Geophysics*, vol. 77, no. 4, pp. H57–H62, 2012.

[23] F. A. Belina, J. Irving, J. R. Ernst, and K. Holliger, "Waveform inversion of crosshole georadar data: Influence of source wavelet variability and the suitability of a single wavelet assumption," *IEEE Trans. Geosci. Remote Sens.*, vol. 50, no. 11, pp. 4610–4625, Nov. 2012.

[24] S. Busch, J. van der Kruk, and H. Vereecken, "Improved characterization of fine-texture soils using on-ground GPR full-waveform inversion," *IEEE Trans. Geosci. Remote Sens.*, vol. 52, no. 7, pp. 3947–3958, Jul. 2014.

[25] I. Giannakis, A. Giannopoulos, and C. Warren, "Realistic FDTD GPR antenna models optimized using a novel linear/nonlinear full-waveform inversion," *IEEE Trans. Geosci. Remote Sens.*, vol. 57, no. 3, pp. 1768–1778, Mar. 2019.

[26] D. J. Daniels, *Ground Penetrating Radar*, 2nd ed. London, U.K.: IET, 2004.

[27] S. J. Ahn, W. Rauh, and H.-J. Warnecke, "Least-squares orthogonal distances fitting of circle, sphere, ellipse, hyperbola, and parabola," *Pattern Recognit.*, vol. 34, no. 12, pp. 2283–2303, Dec. 2001.

[28] L. Mertens, R. Persico, L. Matera, and S. Lambot, "Automated detection of reflection hyperbolas in complex GPR images with NoA prioriknowledge on the medium," *IEEE Trans. Geosci. Remote Sens.*, vol. 54, no. 1, pp. 580–596, Jan. 2016.

[29] Q. Dou, L. Wei, D. R. Magee, and A. G. Cohn, "Real-time hyperbola recognition and fitting in GPR data," *IEEE Trans. Geosci. Remote Sens.*, vol. 55, no. 1, pp. 51–62, Jan. 2017.

[30] L. Capineri, P. Grande, and J. A. G. Temple, "Advanced image-processing technique for real-time interpretation of ground-penetrating radar images," *Int. J. Imag. Syst. Technol.*, vol. 9, no. 1, pp. 51–59, 1998.

[31] C. G. Windsor, L. Capineri, and P. Falorni, "A data pair-labeled generalized Hough transform for radar location of buried objects," *IEEE Geosci. Remote Sens. Lett.*, vol. 11, no. 1, pp. 124–127, Jan. 2014.

[32] W. Al-Nuaimy, Y. Huang, M. Nakhkash, M. T. C. Fang, V. T. Nguyen, and A. Eriksen, "Automatic detection of buried utilities and solid objects with GPR using neural networks and pattern recognition," *J. Appl. Geophys.*, vol. 43, nos. 2–4, pp. 157–165, Mar. 2000.

[33] C. Maas and J. Schmalzl, "Using pattern recognition to automatically localize reflection hyperbolas in data from ground penetrating radar," *Comput. Geosci.*, vol. 58, pp. 116–125, Aug. 2013.

[34] P. Viola and M. J. Jones, "Robust real-time face detection," *Int. J. Comput. Vis.*, vol. 57, no. 2, pp. 137–154, 2004.

[35] T. Russel and C. Cutler, *Trees: An Illustrated Identifier and Encyclopedia*. Leicestershire, U.K.: Hermes House, 2012.

[36] J.-H. Kim, S.-J. Cho, and M.-J. Yi, "Removal of ringing noise in GPR data by signal processing," *Geosci. J.*, vol. 11, pp. 75–81, Mar. 2007.

[37] I. Giannakis, S. Xu, P. Aubry, A. Yarovoy, and J. Sala, "Signal processing for landmine detection using ground penetrating radar," in *Proc. IEEE Int. Geosci. Remote Sens. Symp.*, Jul. 2016, pp. 7442–7445.

[38] I. Giannakis, A. Giannopoulos, C. Warren, and N. Davidson, "Numerical modelling and neural networks for landmine detection using ground penetrating radar," in *Proc. 8th Int. Workshop Adv. Ground Penetrating Radar (IWAGPR)*, Jul. 2015, pp. 1–4.

[39] J. Kennedy and R. Eberhart, "Particle swarm optimization," in *Proc. IEEE Int. Conf. Neural Netw.*, vol. 4, Nov./Dec. 1995, pp. 1942–1948.

[40] R. J. Sharpe and R. W. Thorne, "Numerical method for extracting an arc length parameterization from parametric curves," *Comput.-Aided Des.*, vol. 14, no. 2, pp. 79–81, Mar. 1982.

[41] B. Guenter and R. Parent, "Computing the arc length of parametric curves," *IEEE Comput. Graph. Appl.*, vol. 10, no. 3, pp. 72–78, May 1990.

[42] E. Kreyszig, *Advanced Engineering Mathematics*, 8th ed. New York, NY, USA: Wiley, 1999.

[43] J. Ježová, J. Harou, and S. Lambot, "Reflection waveforms occurring in bistatic radar testing of columns and tree trunks," *Construct. Building Mater.*, vol. 174, pp. 388–400, Jun. 2018.

[44] N. Bonomo, D. Bullo, A. Villela, and A. Osella, "Ground-penetrating radar investigation of the cylindrical pedestal of a monument," *J. Appl. Geophys.*, vol. 113, pp. 1–13, Feb. 2015.

[45] H. Brunzell, "Detection of shallowly buried objects using impulse radar," *IEEE Trans. Geosci. Remote Sens.*, vol. 37, no. 2, pp. 875–886, Mar. 1999.

[46] R. Wu *et al.*, "Adaptive ground bounce removal," *Electron. Lett.*, vol. 37, no. 20, pp. 1250–1252, Sep. 2001.

[47] I. Giannakis, "Realistic numerical modelling of ground penetrating radar for landmine detection," Ph.D. dissertation, Univ. Edinburgh, Scotland, U.K., 2016.

[48] J. Robinson and Y. Rahmat-Samii, "Particle swarm optimization in electromagnetics," *IEEE Trans. Antennas Propag.*, vol. 52, no. 2, pp. 397–407, Feb. 2004.

[49] D. F. Kelley, T. J. Destan, and R. J. Luebbers, "Debye function expansions of complex permittivity using a hybrid particle swarm-least squares optimization approach," *IEEE Trans. Antennas Propag.*, vol. 55, no. 7, pp. 1999–2005, Jul. 2007.

[50] J. L. F. Martínez, E. G. Gonzalo, J. P. F. Álvarez, H. A. Kuzma, and C. O. M. Pérez, "PSO: A powerful algorithm to solve geophysical inverse problems: Application to a 1D-DC resistivity case," *J. Appl. Geophys.*, vol. 71, no. 1, pp. 13–25, May 2010.

[51] A. Taflove and S. C. Hagness, *Computational Electrodynamics: The Finite-Difference Time-Domain Method*, 2nd ed. Norwood, MA, USA: Artech House, 2000.

[52] C. Warren *et al.*, "A CUDA-based GPU engine for gprMax: Open source FDTD electromagnetic simulation software," *Comput. Phys. Commun.*, vol. 237, pp. 208–218, Apr. 2019.

[53] C. Warren, A. Giannopoulos, and I. Giannakis, "gprMax: Open source software to simulate electromagnetic wave propagation for ground penetrating radar," *Comput. Phys. Commun.*, vol. 209, pp. 163–170, Dec. 2016.

[54] T. Douglas, *Effective Dielectric Constants of Foliage Media*, Rome Air Development Center, Griffiss AFB, Rome, NY, USA, 1990.

[55] N. R. Peplinski, F. T. Ulaby, and M. C. Dobson, "Dielectric properties of soils in the 0.3-1.3-GHz range," *IEEE Trans. Geosci. Remote Sens.*, vol. 33, no. 3, pp. 803–807, May 1995.

[56] M. G. Broadhurst, "Complex dielectric constant and dissipation factor of foliage," Nav. Ordnance Lab., Mongomery County, MD, USA, NBS Rep. 9592, Oct. 1970.

[57] G. S. Brown and W. J. Curry, "A theory and model for wave propagation through foliage," *Radio Sci.*, vol. 17, no. 5, pp. 1027–1036, Sep./Oct. 1982.

[58] W. L. James, "Dielectric properties of wood and hardboard: Variation with temperature, frequency, moisture content, and grain orientation," USDA Forest Products Lab., Madison, MI, USA, USDA Forest Service Res. Paper FPL 245, 1975.

[59] J. R. Birchak, C. G. Gardner, J. E. Hipp, and J. M. Victor, "High dielectric constant microwave probes for sensing soil moisture," *Proc. IEEE*, vol. 62, no. 1, pp. 93–98, Jan. 1974.

[60] I. Giannakis and A. Giannopoulos, "A novel piecewise linear recursive convolution approach for dispersive media using the finite-difference time-domain method," *IEEE Trans. Antennas Propag.*, vol. 62, no. 5, pp. 2669–2678, May 2014.

[61] N. J. Brazee, R. E. Marra, L. Göcke, and P. Van Wassenaer, "Nondestructive assessment of internal decay in three hardwood species of northeastern North America using sonic and electrical impedance tomography," *Forestry*, vol. 84, no. 1, pp. 33–39, Dec. 2010.

[62] A. Guyot, K. T. Ostergaard, M. Lenkopane, J. Fan, and D. A. Lockington, "Using electrical resistivity tomography to differentiate sapwood from heartwood: Application to conifers," *Tree Physiol.*, vol. 33, no. 2, pp. 187–194, Feb. 2013.

[63] W. C. Shortle and K. R. Dudzik, *Wood Decay in Living and Dead Trees: A Pictorial Overview*. Washington, DC, USA: United States Forest Service, 2012.

[64] B. Larsson, B. A. Bengtsson, and M. Gustafsson, "Nondestructive detection of decay in living trees," Lund Univ., Lund, Sweden, Tech. Rep. LUTEDX/(TEAT-7111)/1-15/, 2002.

[65] C. Warren and A. Giannopoulos, "Creating finite-difference time-domain models of commercial ground-penetrating radar antennas using Taguchi's optimization method," *Geophysics*, vol. 76, no. 2, pp. G37–G47, Apr. 2011.

[66] C. J. Humphries, J. R. Press, and D. A. Sutton, *Guide to Trees of Britain and Europe*. London, U.K.: Philip, 2006.

[67] M. Spohn and R. Spohn, *Trees of Britain and Europe*. London, U.K.: A & C Black, 2008.

[68] N. Brown, "Epidemiology of acute oak decline in great Britain," Ph.D. dissertation, Imperial College London, London, U.K., 2014.

[69] N. Brown, D. J. G. Inward, M. Jeger, and S. Denman, "A review of *Agrilus biguttatus* in UK forests and its relationship with acute oak decline," *Forestry, Int. J. Forest Res.*, vol. 88, no. 1, pp. 53–63, Jan. 2015.

[70] S. Denman, N. Brown, S. Kirk, M. Jeger, and J. Webber, "A description of the symptoms of acute oak decline in Britain and a comparative review on causes of similar disorders on oak in Europe," *Forestry, Int. J. Forest Res.*, vol. 87, no. 4, pp. 535–551, Oct. 2014.

[71] N. Ahmad, M. Wistuba, and H. Lorenzl, "GPR as a crack detection tool for asphalt pavements: Possibilities and limitations," in *Proc. 14th Int. Conf. Ground Penetrating Radar (GPR)*, Shanghai, China, Jun. 2012, pp. 551–555.

[72] S. Lameri, F. Lombardi, P. Bestagini, M. Lualdi, and S. Tubaro, "Landmine detection from GPR data using convolutional neural networks," in *Proc. 25th Eur. Signal Process. Conf.*, Kos, Greece, Aug./Sep. 2017, pp. 508–512.

Iraklis Giannakis received the bachelor's and master's degrees in geophysics from the Aristotle University of Thessaloniki, Thessaloniki, Greece, in 2009 and 2011, respectively, and the Ph.D. degree from The University of Edinburgh, Edinburgh, Scotland, through a project cofunded by the Defense Science and Technology Laboratory, U.K., and the Engineering and Physical Sciences Research Council, U.K.

He is currently a Research Fellow with the School of Computing and Engineering, University of West London, London, U.K., where he has been involved in applications of ground-penetrating radar (GPR) to sustainable management of forestry heritage. His research interests include near-surface geophysics, nondestructive testing, computational electromagnetics, and machine learning.

Dr. Giannakis was a recipient of the Best Paper Award at the 15th International Conference on GPR in 2014.

Fabio Tosti (M'17–SM'19) received the M.Sc. engineering degree *(cum laude)* in infrastructure and transportation engineering and the Ph.D. degree (Hons.) from Rome Tre University, Rome, Italy, in 2010 and 2014, respectively.

He is currently an Associate Professor in civil engineering and the Deputy Head of The Faringdon Center—The Non-destructive Testing Center, University of West London, London, U.K. He has authored or coauthored more than 120 research publications in international journals, conferences, and books. His research interests include the development of new algorithms, methodologies, and numerical models for geoscience applications and the nondestructive assessment, repair, and maintenance of civil engineering infrastructures.

Dr. Tosti was a recipient of the Early Career Scientists Award by the European Geosciences Union (EGU) for his outstanding contribution to the development of new GPR methodologies in geosciences and civil engineering in 2017. He served as an Organizer, as a Panel Member (Scientific), and as the Session Chair in several international conferences. He held a supervisory role at the International Project European Cooperation in Science and Technology TU1208 Action, titled "Civil Engineering Applications of Ground Penetrating Radar." He holds the position of Convener at the EGU General Assembly for sessions on nondestructive testing methods and data fusion. He has served as an Associate and Managing Guest Editor in numerous international journals.

Livia Lantini received the B.Sc. (Hons.) degree in civil engineering and the M.Sc. degree in infrastructure and transportation engineering with the Department of Engineering, Rome Tre University, Rome, Italy. She is currently pursuing the Ph.D. degree with the School of Computing and Engineering, University of West London, London, U.K.

Her research interests include assessment and health monitoring of trees and the investigation of tree roots and soil interaction using ground penetrating radar and other nondestructive methods.

Amir M. Alani was the Rochester Bridge Trust Professor of engineering with the University of West London, London, U.K., in 2018, where he has been the Executive Dean of the School of Computing and Engineering since 2014. He currently leads the Faringdon Center—The Non-Destructive Research Center, University of West London. He is an expert in the assessment, repair, and maintenance of civil engineering infrastructures such as bridges, tunnels, and buildings and has extensive work experience with different professional bodies in the fields of engineering and design both in the U.K. and Europe. He has more than 25 years of work experience in higher education and industry in the U.K. He was involved in the research and development of different branches of civil and mechanical engineering, including the applications of nondestructive testing methods, concrete technology, geotechnics and soil engineering, and engineering education. He has authored or coauthored more than 180 journal papers, book chapters, international conference papers, and consulting external reports in these areas.

Dr. Alani was a Management Committee Member for a European Cooperation in Science and Technology (COST) Action project, TU1208 Project 2012-2017, "Civil Engineering Applications of Ground Penetrating Radar (GPR)." He has delivered and led numerous seminars and workshops nationally and internationally, and has chaired a number of international conference sessions in the past 20 years.